A Circuit Analysis of Pre-Emphasis Pulses for RC Delay Lines

PAPER

A Circuit Analysis of Pre-Emphasis Pulses for RC Delay Lines

Kazuki MATSUYAMA[†*], ***Nonmember and*** **Toru TANZAWA**[†a)], ***Member***

SUMMARY This paper formulates minimal word-line (WL) delay time with pre-emphasis pulses to design the pulse width as a function of the overdrive voltage for large memory arrays such as 3D NAND. Circuit theory for a single RC line only with capacitance to ground and that only with coupling capacitance as well as a general case where RC lines have both grounded and coupling capacitance is discussed to provide an optimum pre-emphasis pulse width to minimize the delay time. The theory is expanded to include the cases where the resistance of the RC line driver is not negligibly small. The minimum delay time formulas of a single RC delay line and capacitive coupling RC lines was in good agreement (i.e. within 5% error) with measurement. With this research, circuit designers can estimate an optimum pre-emphasis pulse width and the delay time for an RC line in the initial design phase.

key words: *pre-emphasis, RC delay, delay time, NAND flash, flat panel display, word-line, column-line*

Nomenclature

T_{pre}	: Pre-emphasis time
T_{opt}	: Optimum T_{pre} to minimize the delay time
E	: Target voltage
α	: Rate of the pre-emphasis voltage to E
β	: Error rate to E
γ	: Model dependent parameter
x	: Delay line position ($x = 0$ for the nearest, $x = l$ for the farthest)
r	: Resistance per unit length
c_g	: Ground capacitance per unit length
c_c	: Coupling capacitance per unit length
R	: Resistance
C_g	: Ground capacitance
C_c	: Coupling capacitance
e	: Natural logarithm
$e(x,t)$	: Voltage at a position x and a time t
$i(x,t)$	: Current at a position x and a time t
$E(x,s)$	: Laplace transform of $e(x,t)$ with respect to t
$I(x,s)$	: Laplace transform of $i(x,t)$ with respect to t
t_{delay_min}	: Minimal time for the slowest node voltage to reach βE
R_d	: Driver resistance or source resistance

1. Introduction

Pre-emphasis pulses have been widely used to reduce wire delays in integrated circuit (IC) designs as illustrated in Fig. 1. High speed design for interconnection modeled by an LC line between a driver chip and a receiver chip requires to compensate inter-symbol interference with a programmable pre-emphasis pulse [1]. The driving current of

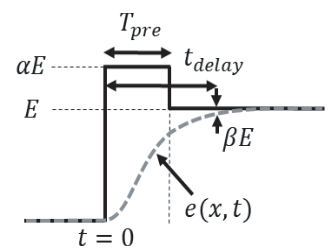

Fig. 1 Pre-emphasis pulse and the definition of the design parameters.

output buffers was controlled depending on previous output data. In [2], the pre-emphasis pulse was used for column drivers in flat panel displays with compensation for process variation. Prior to user modes, various pre-emphasis pulses were tested to find the best design parameters of the pulses for minimal column delay time. One of the design challenges in 3D NANDs is the larger word-line (WL) loading compared to that of planar devices [3], [4]. In [3], WL resistance is measured by using monitoring blocks. By applying the proper voltage and set-up time of a pre-emphasis pulse based on the measured average WL resistance, WL setup time can be minimized even with large process variation as far as within-die variation in WL resistance is much less than die-by-die variation. It was shown that WL rise time was reduced by 45% and the total read time, tR, was 45 µs in a 128 Gb TLC 3D NAND in [3]. When bit-line access time is assumed to be 15 µs, the WL delay time can be estimated to be 50 µs without pre-emphasis pulses and 30 µs with pre-emphasis pulses. As a result, the reduction in the total read time with pre-emphasis pulses can be as large as 30%. In addition, in the memory and display circuits, the pre-emphasis waveform can be controlled by updating the digital code for digital-to-analog converters of WL and column-line (CL) drivers [5], eliminating the need for an additional circuit. WLs and CLs are modeled by RC delay lines because wires are fabricated with thin film poly-silicon and tungsten layers. Thus, pre-emphasis is a key design technique to minimize RC delay lines such as WLs and CLs.

Wire delay time has been theoretically analyzed only for step pulses [6]–[10]. In [7], closed-form solutions were presented for voltage- step response of open and shorted distributed RC lines. In [8] and [9], approximated wiring delay was described to estimate the delay time for a single RC line and coupled ones, respectively, when a step pulse was applied. In [10], coupling noise was formulated for distributed RC lines driven by a step pulse. In [11]–[14], various RC

Manuscript received July 10, 2020.
Manuscript revised August 19, 2020.
Manuscript publicized November 24, 2020.
[†]The author is with Shizuoka University, Hamamatsu-shi, 432-8561 Japan.
[*]Presently, with Fuji Corp.
a) E-mail: toru.tanzawa@shizuoka.ac.jp
DOI: 10.1587/transfun.2020EAP1083

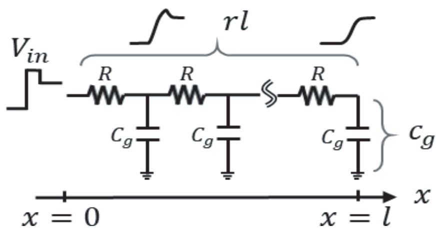

Fig. 2 Equivalent circuit of single RC delay line (WL or CL).

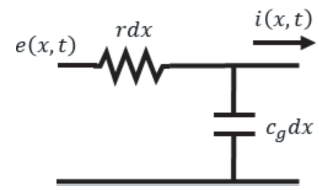

Fig. 3 Distributed element model of a single RC line.

models were introduced to calculate non-electrical systems such as biological reaction–diffusion phenomena and compositional changes in dielectric materials. However, a general optimization method for the pre-emphasis pulses has not been formulated in literature to the best of the knowledge of the authors. In [15], we formulated the optimum pre-emphasis pulse design conditions, minimum delay time, power consumption, and production error effects in the simplest single RC delay line with only ground capacitance as shown in Fig. 2. An increase in energy associated with a pre-emphasis pulse for WL in 3D NAND can be estimated to be as low as a few percent according to [15]. In addition, in the case of a capacitive coupling RC lines without ground capacitance as shown in Fig. 4, it was shown that the optimal parameters could be calculated by converting the original circuit into a simplified equivalent circuit and performing the same type of calculation as for the single RC delay line. For the case with driver resistance as shown in Fig. 20, an approximation formula was derived by applying the concept of Elmore delay [6]. In [16], a cost-effective pre-emphasis pulse generator is proposed to eliminate additional monitoring circuits required in [3] or additional calibration operation used in [4], based on the circuit theory discussed in [15].

In this paper, the circuit theory on pre-emphasis pulses is generalized to include both ground and coupling capacitance as in actual memory and display arrays. The generalized circuit theory includes the results for $c_c = 0$ and $c_g = 0$ as described in [15] as extreme conditions. The analytical results are validated by comparing simulated and measured results. In addition, since the error rate of the approximate expression when including the driver resistance was relatively large in [15], the empirical expression is derived using the SPICE simulation results. This paper is organized as follows. In Sect. 2, we derive the circuit theory on general RC lines, single RC lines and capacitive coupling RC lines. Section 3 compares the derived formula with measured and simulated results and derives empirical equations for single RC lines with driver resistance. Section 4 gives a summary.

2. Circuit Theory

This section formulates circuit theory on a single RC line with negligibly small Cc in Sect. 2.1, three unique lines with negligibly small Cg in Sect. 2.2, and three general lines with both Cg and Cc considered in Sect. 2.3. The key analysis for the former two cases was presented in [15]. In this paper, the formulation will be described in more detail not only for the former two cases, but also newly for the last one. As will be shown in Sect. 3.6, the general three-line model is valid for such a wide range as $0.5 < Cc/Cg < 10$. A single line model and thee-line model are valid only for $Cc/Cg < 0.5$ and for $Cc/Cg > 10$, respectively. Thus, the work presented in this paper can cover the design space much wider than [15] does.

2.1 Single RC Line

In this section, the optimum parameter for the pre-emphasis waveform and the minimum delay time are calculated for the circuit shown in Fig. 2 with R and C_g. In actual circuits, circuit parameters may not be uniform across the RC line due to process variation. However, as will be shown in Sect. 3, the effects of the process variation on design equations is sufficiently small. In [15], the same circuit is used for derivation, but we will discuss the theory with more detailed explanation and compare it with the three general RC lines. First, we calculate the voltage waveform at each position and time when a pre-emphasis pulse is input to the circuit. An element of Fig. 2 is shown in Fig. 3. Circuit equations are given by (1) and (2).

$$-\frac{\partial e(x,t)}{\partial x} = ri(x,t) \tag{1}$$

$$-\frac{\partial i(x,t)}{\partial \mathrm{x}} = c_g \frac{\partial e(x,t)}{\partial \mathrm{t}} \tag{2}$$

Simultaneous partial differential equation of (1) and (2) can be solved exactly to be (3) and (4) when the initial and boundary conditions of $e(x,0) = i(x,0) = 0, e(0,t) = V_{in}$ and $i(l,t) = 0$ are used, which indicates the RC line is fully discharged at $t = 0$, the input terminal is driven by V_{in} (see Fig. 1), and the current at the farthest point ($x = l$) is 0 at any time because of no further element beyond $x = l$.

$$e(x,t) = \alpha E - \frac{4\alpha E}{\pi}\sum_{k=0}^{\infty}\frac{1}{2k+1}e^{\frac{-(2k+1)^2}{\tau_1}t}sin\frac{(2k+1)\pi x}{2l} \qquad 0 \le \mathrm{t} \le T_{pre} \tag{3}$$

$$e(x,t) = E - \frac{4E}{\pi}\sum_{k=0}^{\infty}\left\{\alpha - (\alpha-1)e^{\frac{(2k+1)^2}{\tau_1}T_{pre}}\right\} \cdot \frac{1}{2k+1}e^{\frac{-(2k+1)^2}{\tau_1}t}sin\frac{(2k+1)\pi x}{2l} \qquad \mathrm{t} > T_{pre} \tag{4}$$

where τ_1 is a time constant given by $\tau_1 = 4rc_g l^2/\pi^2$. Appendix A shows the calculation procedure. (3) and (4) are, respectively, the solutions in (A·10) and (A·23). (3) is the same as the result in [8] when a step pulse is input to a single RC line. Let's determine the optimum $T_{pre}(T_{opt})$ which minimizes the delay time. When one focuses on the case where $\beta \ll 10\%$, the delay time would be much longer than τ_1. For $t \gg \tau_1$, (4) can be approximated as (5)

$$e(x,t) \fallingdotseq E + A_0\left(x, T_{pre}\right)\mathrm{e}^{\frac{-t}{\tau_1}} + A_1\left(x, T_{pre}\right)e^{\frac{-9t}{\tau_1}} \tag{5}$$
$$A_0\left(x, T_{pre}\right) = -\frac{4E}{\pi}\left\{\alpha - (\alpha-1)e^{\frac{T_{pre}}{\tau_1}}\right\}\cdot sin\frac{\pi x}{2l}$$
$$A_1\left(x, T_{pre}\right) = -\frac{4E}{\pi}\left\{\alpha - (\alpha-1)e^{\frac{9T_{pre}}{\tau_1}}\right\}\cdot \frac{1}{3}sin\frac{3\pi x}{2l}$$

where A_0 and A_1 are the proportional coefficients for the first two dominant factors. Because $e^{-9t/\tau_1} \ll e^{-t/\tau_1}$, one can approximately minimize the delay time with $A_0\left(x, T_{opt}\right) = 0$. Thus:

$$T_{opt} \approx \tau_1 ln\frac{\alpha}{\alpha-1} \tag{6}$$

And (5) becomes (7) with (6).

$$e(x,t) \fallingdotseq E + A_1\left(x, T_{opt}\right)e^{\frac{-9t}{\tau_1}} \tag{7}$$

The equation $E - e\left(x, t_{delay}(x)\right) = \beta E$ with (7) becomes (8)

$$t_{delay}(x) \approx \frac{\tau_1}{9}ln\left|\frac{4\alpha}{3\pi\beta}\left\{\left(\frac{\alpha}{\alpha-1}\right)^8 - 1\right\}sin\frac{3\pi x}{2l}\right| \tag{8}$$

(8) is maximized at $x = l, l/3$. When $[\alpha/(\alpha-1)]^8 \gg 1$, (8) becomes (9), which provides the minimal delay time as a function of α and β.

$$t_{delay\_min} \approx \frac{\tau_1}{9}\ln\left[\frac{4\alpha}{3\pi\beta}\left(\frac{\alpha}{\alpha-1}\right)^8\right] \tag{9}$$

As a result, one can easily determine T_{opt} and t_{delay_min} by using (6) and (9) for single RC lines.

2.2 Three Unique RC Lines

In 3D NANDs, the capacitance between adjacent WLs is dominant [3], [4], and can be modeled as three RC delay lines as shown in Fig. 4. In [15], we showed that the transient response in such a circuit could be calculated using circuit transformation. This section introduces the calculation procedure. Because of its symmetry, the potential of adjacent lines at the same location x are equal when all three lines are fully discharged at $t = 0$. As a result, Fig. 4 can be reduced to Fig. 5. Each element is shown in Fig. 6.

Note that in Fig. 5, GND is only at the input ($x = 0$), so the current in the adjacent line is equal to that in the target line. Simultaneous partial differential equations for $e_1(x,t)$, $e_2(x,t)$ and $i(x,t)$ are, respectively:

$$-\frac{\partial e_1(x,t)}{\partial x} = ri(x,t) \tag{10}$$
$$-\frac{\partial e_2(x,t)}{\partial x} = -\frac{r}{2}i(x,t) \tag{11}$$

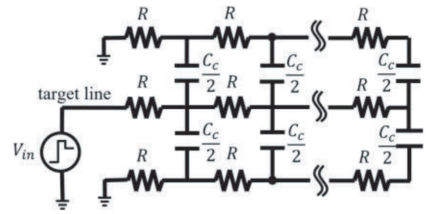

Fig. 4 Equivalent circuit of capacitive coupling RC lines.

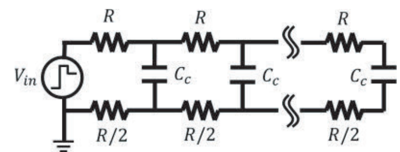

Fig. 5 Equivalent circuit of Fig. 4.

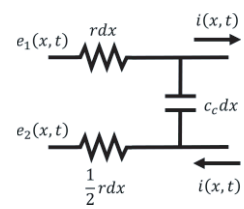

Fig. 6 Distributed element model of capacitive coupling RC lines.

$$-\frac{\partial i(x,t)}{\partial x} = c\frac{\partial\left[e_1(x,t) - e_2(x,t)\right]}{\partial t} \tag{12}$$

When $e_1(x,t) - e_2(x,t) = e_3(x,t)$, these expressions can be written as:

$$-\frac{\partial e_3(x,t)}{\partial x} = 1.5ri(x,t) \tag{13}$$
$$-\frac{\partial i(x,t)}{\partial x} = c\frac{\partial e_3(x,t)}{\partial t} \tag{14}$$

Since those equations have the similar forms to (1) and (2) for the single RC lines, $e_3(x,t)$ can be obtained by the same procedure as Appendix A. From (10), (11) and (13), the relationship (15) can be obtained.

$$\frac{\partial e_1(x,t)}{\partial x} = -2\frac{\partial e_2(x,t)}{\partial x} = \frac{2}{3}\frac{\partial e_3(x,t)}{\partial x} \tag{15}$$

Equations (10), (11) and (12) can be solved exactly to be (16) or (17) when the initial and boundary conditions of $e_1(x,0) = e_2(x,0) = i(x,0) = 0$, $e_1(0,t) = V_{in}$, $e_2(0,t) = 0$ and $i(l,t) = 0$ are used, which indicates the RC lines are fully discharged at $t = 0$, the input terminal is driven by V_{in} (see Fig. 1), the input terminal of the adjacent line is ground and the current at the farthest point ($x = l$) is 0 at any time because of no further element beyond $x = l$.

$$e_1(x,t) = \alpha E - \frac{8\alpha E}{3\pi}\sum_{k=0}^{\infty}\frac{1}{2k+1}e^{\frac{-(2k+1)^2}{1.5\tau_2}t}sin\frac{(2k+1)\pi x}{2l}$$
$$0 \le t \le T_{pre} \tag{16}$$

$$e_1(x,t) = E - \frac{8E}{3\pi}\sum_{k=0}^{\infty}\left\{\alpha - (\alpha-1)e^{\frac{(2k+1)^2}{1.5\tau_2}T_{pre}}\right\}$$

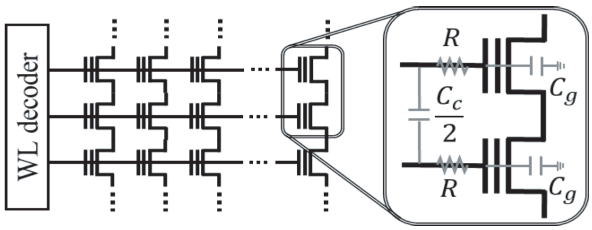

Fig. 7 Parasitic elements of 3D NAND flash memory.

$$\cdot\frac{1}{2k+1}e^{\frac{-(2k+1)^2}{1.5\tau_2}t}sin\frac{(2k+1)\pi x}{2l} \qquad T_{pre} < t \tag{17}$$

where τ_2 is a time constant given by $\tau_2 = 4rc_cl^2/\pi^2$. The minimal delay condition and minimal delay time are calculated to be (18) and (19), respectively, with the same procedure as the single RC lines.

$$T_{opt} \approx 1.5\tau_2 ln\frac{\alpha}{\alpha-1} \tag{18}$$

$$t_{delay\_min} \approx \frac{1.5\tau_2}{9}ln\left[\frac{4\alpha}{3\pi\beta}\left(\frac{\alpha}{\alpha-1}\right)^8\right] \tag{19}$$

As a result, one can easily determine T_{opt} and t_{delay_min} by using (18) and (19) for three parallel lines without c_g.

2.3 Three General RC Lines

Figure 7 shows a structure of 3D NAND flash memory. It includes a parasitic resistance R, coupling capacitance C_c, and ground capacitance C_g. The capacitance between adjacent WLs is expressed as $C_c/2$. Considering all the parasitic elements in Fig. 7, the WL decoder needs to drive an equivalent circuit as shown in Fig. 8. One may want to have 5 or more WLs in a model for higher accuracy, but as will be shown in Sect. 3, the impact of additional WLs on delay performance is minimal. Let's derive the voltage waveform at each position and time when a pre-emphasis pulse is input to the three general RC lines. Because of their symmetry, the potential of adjacent lines at the same location x are equal when all three lines are fully discharged at $t = 0$. As a result, Fig. 8 can be reduced to Fig. 9. An element of Fig. 9 is shown in Fig. 10. Simultaneous partial differential equations for $e_1(x,t)$, $e_2(x,t)$, $i_1(x,t)$ and $i_2(x,t)$ are composed of (20)–(23) as follows.

$$-\frac{\partial e_1(x,t)}{\partial x} = ri_1(x,t) \tag{20}$$

$$-\frac{\partial e_2(x,t)}{\partial x} = \frac{1}{2}ri_2(x,t) \tag{21}$$

$$-\frac{\partial i_1(x,t)}{\partial x} = c_c\frac{\partial\left[e_1(x,t)-e_2(x,t)\right]}{\partial t} + c_g\frac{\partial e_1(x,t)}{\partial t} \tag{22}$$

$$-\frac{\partial i_2(x,t)}{\partial x} = -c_c\frac{\partial\left[e_1(x,t)-e_2(x,t)\right]}{\partial t} + 2c_g\frac{\partial e_2(x,t)}{\partial t} \tag{23}$$

As shown in Appendix B, Eqs. (20), (21), (22) and (23) can be solved exactly to be (A·41) and (A·60), or (24) and

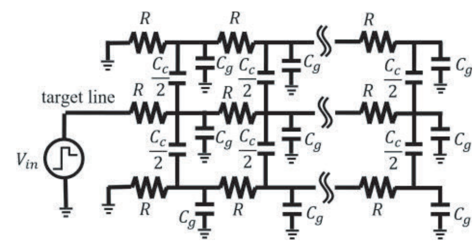

Fig. 8 Equivalent circuit of general three RC lines.

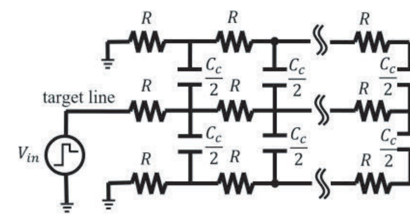

Fig. 9 Equivalent circuit of Fig. 8.

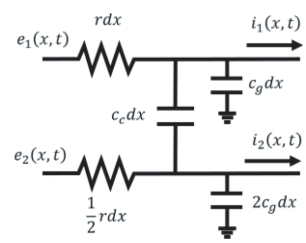

Fig. 10 Distributed element model of general three RC lines.

(25), when the initial and boundary conditions of $e_1(x,0) = e_2(x,0) = i_1(x,0) = i_2(x,0) = 0$, $e_1(0,t) = V_{in}$, $e_2(0,t) = 0$ and $i_1(l,t) = i_2(l,t) = 0$ are used, which indicate the RC lines are fully discharged at $t = 0$, the input terminal is driven by V_{in} (see Fig. 1), the input terminal of the adjacent line is ground and the current at the farthest point ($x = l$) is 0 at any time because of no further element beyond $x = l$.

$$\begin{aligned} e_1(x,t) = \alpha E &- \frac{8\alpha E}{3\pi}\sum_{k=0}^{\infty}\frac{1}{2k+1}e^{\frac{-(2k+1)^2}{\tau_3}t}sin\frac{(2k+1)\pi}{2l}x \\ &- \frac{4\alpha E}{3\pi}\sum_{k=0}^{\infty}\frac{1}{2k+1}e^{\frac{-(2k+1)^2}{\tau_1}t}sin\frac{(2k+1)\pi}{2l}x \\ &\qquad 0 \le t \le T_{pre} \end{aligned} \tag{24}$$

$$\begin{aligned} e_1(x,t) = E &- \frac{8E}{3\pi}\sum_{k=0}^{\infty}\left\{\alpha-(\alpha-1)e^{\frac{(2k+1)^2}{\tau_3}T_{pre}}\right\} \\ &\cdot\frac{1}{2k+1}e^{\frac{-(2k+1)^2}{\tau_3}t}sin\frac{(2k+1)\pi}{2l}x \\ &- \frac{4E}{3\pi}\sum_{k=0}^{\infty}\left\{\alpha-(\alpha-1)e^{\frac{(2k+1)^2}{\tau_1}T_{pre}}\right\} \\ &\cdot\frac{1}{2k+1}e^{\frac{-(2k+1)^2}{\tau_1}t}sin\frac{(2k+1)\pi}{2l}x \\ &\qquad T_{pre} < t \end{aligned} \tag{25}$$

where $\tau_3 = 4r\left(1.5c_c + c_g\right)l^2/\pi^2$ and $\tau_1 = 4rc_gl^2/\pi^2$. By substituting $c_c = 0$ into these equations, single line Eqs. (6)

and (9) can be obtained. By substituting $c_g = 0$, three-line Eqs. (16) and (17) can be obtained. Therefore, (24) and (25) includes the solutions (6) and (9) for single RC lines and the solutions (16) and (17) for three unique RC lines.

Let's determine the optimum $T_{pre}(T_{opt})$ which minimizes the delay time. In the case of a single RC line, there was only one time constant. As a result, it is possible to analytically calculate the optimum value. However, since (24) and (25) have two time constants, it is impossible to analytically solve the equation with respect to t. Instead, we numerically determined T_{opt} and the minimum delay time. Based on T_{opt} and t_{delay_min} for the single RC line of (6) and (9) or those for the thee unique RC lines (18) and (19), we assumed that T_{opt} and t_{delay_min} could be similarly expressed as (26) and (27) where γ_1 and γ_2 are scaling parameters which only depend on C_c/C_g and α where $\tau_4 = 4r\left(c_c + c_g\right) l^2/\pi^2$. Note that $\tau_4 = \tau_1$ and $\gamma_1 = \gamma_2 = 1$ when $c_c = 0$; $\tau_4 = \tau_2$ and $\gamma_1 = \gamma_2 = 1.5$ when $c_g = 0$.

$$T_{opt} \approx \gamma_1 \tau_4 ln \frac{\alpha}{\alpha - 1} \tag{26}$$

$$t_{delay\_min} \approx \gamma_2 \frac{\tau_4}{9} \ln\left[\frac{4\alpha}{3\pi\beta}\left(\frac{\alpha}{\alpha - 1}\right)^8\right] \tag{27}$$

Numerical calculation procedure was done as follows. Under the condition that α, c_c and c_g in (24) and (25) are given, the value of T_{pre} is changed. T_{opt} is determined to have t_{delay_min} ($\beta = 0.01$). Tables 1 and 2 show the results of γ_1 and γ_2 that minimize the delay time for each α and C_c/C_g. γ_1 has little dependency on α. As C_c/C_g increases, it gradually approaches 1.5. In contract, γ_2 has a larger dependency on α than γ_1 does. In particular, in the vicinity of $\alpha = 2$ and $C_c/C_g = 1$, there is a rapid change in γ_2. This is because when the values of C_c and C_g are close, the amount of charge transfer between C_c and C_g increases. As a result, overshoot or undershoot in the voltage waveform greater than β occurs and it takes more time to converge. It is also found that when $C_c/C_g \leq 0.5$, $\gamma_1 \approx 1$. This means that even if C_c is present, T_{opt} can be calculated as a single RC line. These tables are valid only when β is 0.01. For cases of $\beta \neq 0.01$, one needs to build tables similar to Tables 1 and 2 using (24) and (25). Since T_{opt} has a small dependence on β as shown in Sect. 3, an approximate value can be obtained using Table 1. However, since t_{delay} has a large dependence on β, the value cannot be calculated using Table 2 for $\beta \neq 0.01$. One can design an optimum pre-emphasis pulse width T_{opt} with (26) with RC parameters, α and γ_1 in Table 1. Then, one can have a delay time t_{delay_min} with γ_2 as given by Table 2.

Table 1 γ_1 parameters for $\beta = 0.01$.

γ_1		c_c/c_g							
		16	8	4	2	1	0.5	0.25	0.125
α	1.1	1.45	1.37	1.29	1.19	1.08	1.03	1.01	1.00
	1.2	1.46	1.40	1.31	1.21	1.09	1.01	1.00	1.00
	1.3	1.47	1.42	1.32	1.22	1.10	1.01	1.00	1.00
	1.4	1.47	1.42	1.33	1.23	1.10	1.00	1.00	1.00
	1.5	1.47	1.43	1.33	1.23	1.10	1.01	1.00	1.00
	1.6	1.47	1.43	1.34	1.23	1.10	1.01	1.00	1.00
	1.7	1.47	1.43	1.34	1.24	1.11	1.01	1.00	1.00
	1.8	1.47	1.43	1.34	1.24	1.11	1.01	1.00	1.00
	1.9	1.47	1.43	1.34	1.24	1.11	1.01	1.00	1.00
	2	1.47	1.43	1.34	1.24	1.11	1.01	1.00	1.00

Table 2 γ_2 parameters for $\beta = 0.01$.

γ_2		c_c/c_g							
		16	8	4	2	1	0.5	0.25	0.125
α	1.1	1.42	1.36	1.28	1.19	1.07	1.02	1.01	1.00
	1.2	1.44	1.38	1.31	1.24	1.11	1.02	1.01	1.00
	1.3	1.43	1.39	1.32	1.28	1.16	1.01	1.00	1.00
	1.4	1.43	1.38	1.33	1.31	1.20	1.01	1.00	1.00
	1.5	1.42	1.38	1.34	1.34	1.25	1.02	1.00	1.00
	1.6	1.42	1.38	1.34	1.37	1.29	1.03	1.00	1.00
	1.7	1.42	1.38	1.35	1.40	1.34	1.04	1.00	1.00
	1.8	1.42	1.38	1.35	1.43	1.37	1.05	1.00	1.00
	1.9	1.41	1.38	1.36	1.45	1.40	1.06	1.00	1.00
	2	1.41	1.38	1.36	1.47	1.43	1.06	1.00	1.00

3. Validation

In this section, the expression obtained in Sect. 2 is evaluated. A single RC line, capacitive coupling RC lines and three general RC lines were evaluated with measured results of fabricated circuits. Figure 11(a), (b), and (c) shows a chip photograph of a single RC line, that of capacitive coupling RC lines, and a chip layout of three general RC lines instead of a photograph due to lack of photograph because all the fabricated chips have been packaged unfortunately, respectively. The test circuits were fabricated in a 0.18 µm 3 V CMOS. Poly resistors and MIM capacitors were used. Internal nodes are monitored by unity gain buffers. The parameters used in the test circuits are summarized in Table 3. In this experiment, resistors with resistance of an order of MΩ were used to compare measured data with simulated ones precisely.

Even though the R and C values are well controlled by a foundry within a maximum tolerance of 10%, respectively, those values should be measured by die for reliable validation. However, the test structure of a MIM capacitor was too small to extract its capacitance value from the total capacitance including both the capacitance of the MIM capacitor and the parasitic pad capacitance, unfortunately. All the theoretical voltage waveforms after $t = T_{pre}$ such as (4), (17) and (25) only contain the time constant RC rather than individual R and C values. Therefore, it is sufficient to know the actual RC time constant for validation. The RC time constant was extracted from the test structure of a distributed single RC line on the same die as the measured circuit in such a way that the theoretical response (3) of a step pulse

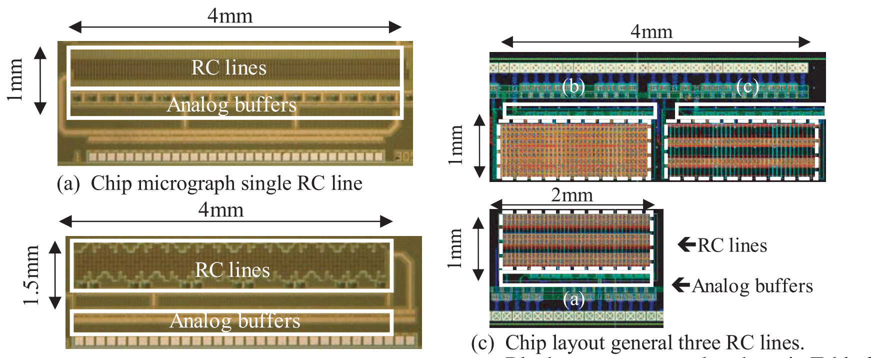

(a) Chip micrograph single RC line

(b) Chip micrograph capacitive coupling RC lines

(c) Chip layout general three RC lines. Blocks a–c correspond to those in Table 3.

Fig. 11 Chip micrographs (a), (b) and chip layout (c).

Table 3 Target RC values used in the test circuits.

		rl	$c_g l$	$c_c l$
Single line		7.7MΩ	194pF	-
Three coupled lines		1.8MΩ	-	173pF
Three general lines	(a)	1.98MΩ	43.2pF	10.8pF
	(b)	1.98MΩ	43.2pF	43.2pF
	(c)	1.98MΩ	10.8pF	43.2pF

input has the same rise time from 0% to 50% of the target voltage as the measured voltage waveform at the far end of the RC line does, where the theoretical response (3) is well known as described in [8]. This method is not as good as individual measurement of R and C, but should be considered good enough to validate the theoretical results using the well-known RC response of a step pulse (3). Thus, the measured waveforms were compared with the theoretical ones whose RC values were extracted as mentioned above.

As will be shown in Figs. 15–17, the minimum delay time decreases as α increases. The upper bound of α is determined by the breakdown voltage of the decoding transistors to select WL or CL. Thus, there is a trade-off in α between the delay time and the reliability of transistors. To measure the waveform, α of 1,6 was used for demonstration.

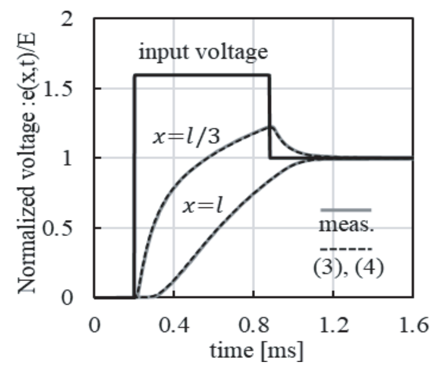

Fig. 12 Measured single RC line.

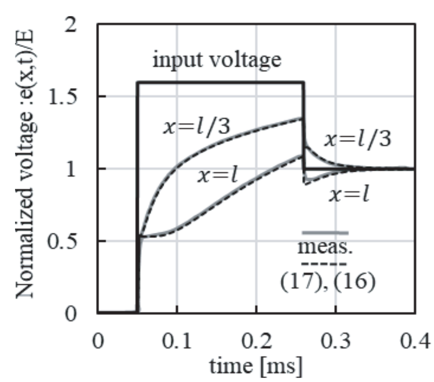

Fig. 13 Measured capacitive coupling RC lines.

3.1 Verification of Output Voltage Waveform

Figure 12 shows the comparison of the measurement results with (3) and (4) for the single RC line when a pre-emphasis pulse that minimizes the delay time is input. Measurements were made at the positions of $x = l$ and $x = l/3$ where the delay time was at a maximum. The gray solid line for the measured value and the dotted line for the formula are in good agreement. It is proved that the formulas (3) and (4) can be derived accurately. It was also confirmed that $x = l$ and $x = l/3$ were the worst cases for delay time. Fig. 13 shows the comparison of the measurement results with (16) and (17) for the capacitive coupling RC lines when a pre-emphasis pulse that minimizes the delay time is input. Measurements were made at the positions of $x = l$ and $x = l/3$ where the delay time was at a maximum. The gray solid line for the measured value and the dotted line for the formula agreed well except when the signal changed. The error at the time of the signal change is due to the parasitic capacitance to ground which is not considered in the model, but it does slightly affect the delay time. It was also confirmed that $x = l$ and $x = l/3$ were the worst cases of the delay time as in the case of the capacitive coupling RC lines. Figure 14 shows the comparison of the measured results with (24) and (25) for the three general RC lines in two patterns: $C_c/C_g = 0.25$ (a) and $= 4$ (b). A pre-emphasis pulse that

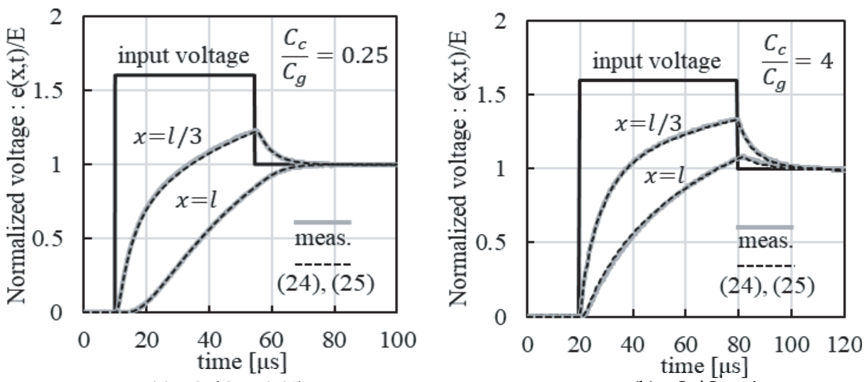

(a): $C_c/C_g = 0.25$ (b): $C_c/C_g = 4$

Fig. 14 Measured general three RC lines.

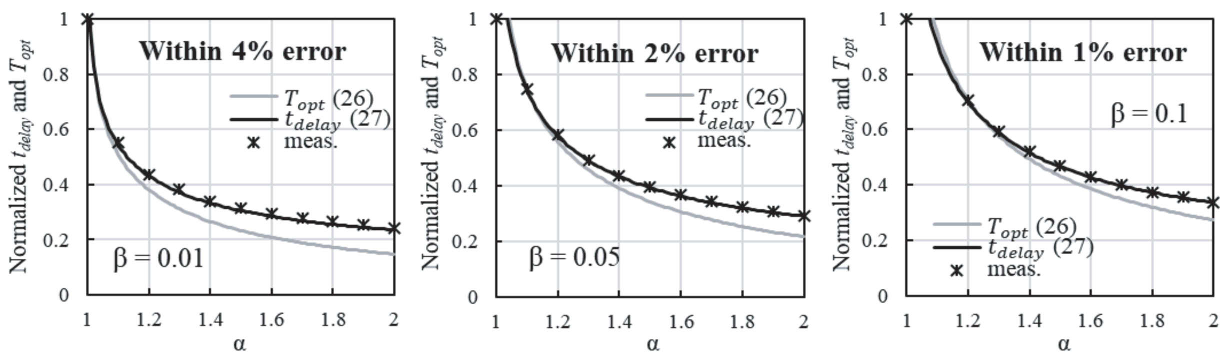

(a): β = 0.01 (b): β = 0.05 (c): β = 0.1

Fig. 15 Verification of t_{delay} in single RC line.

minimizes the delay time was input. Measurements were made at the positions of $x = l$ and $x = l/3$ as with the single RC line and capacitive coupling RC lines. Note that the delay times at positions $x = l$ and $x = l/3$ are not always the worst case for the three general RC lines. The gray solid line for measurement and the dotted line for the formula are in good agreement. It is shown that the formulas (24) and (25) can be derived accurately. When $C_c/C_g = 0.25$, the shape is similar to that of a single RC line; this can also be seen in Tables 1 and 2.

3.2 Verification of T_{opt} and Minimum Delay Time

Figure 15 shows T_{opt} and t_{delay_min} as a function of α for (a) β = 0.01, (b) β = 0.05, and (c) β = 0.1 on a single RC line. The vertical axis is normalized by t_{delay_min} with $\alpha = 1$ in case of a step pulse. Note that the case of α = 1.1, β = 0.1 is not plotted because the error rate is larger than the overdrive voltage and there is no optimal T_{pre}. In Fig. 15(a), the error is within 4% when α ≥ 1.1. In Fig. 15(b), the error is within 2% when α ≥ 1.1; and in Fig. 15(c), the error is within 1% when α ≥ 1.2. When the case of α = 1.6 is compared, the delay time is reduced by 71% when β = 0.01, 63% when β = 0.05, and 57% when β = 0.1. It was found that the effect of pre-emphasis pulsing increases as β decreases. Fig. 16 shows T_{opt} and t_{delay_min} as a function of α for (a) β = 0.01, (b) β = 0.05, and (c) β = 0.1 on capacitive coupling RC lines. The vertical axis is normalized by t_{delay_min} with α = 1 in the case of a step pulse. In Fig. 16(a), the error is within 4% when α ≥ 1.1, in Fig. 16(b), the error is within 4% when α ≥ 1.1, and in Fig. 16(c), the error is within 5% when α ≥ 1.2. When the case of α = 1.6 is compared, the delay time is reduced by 71% when β = 0.01, 61% when β = 0.05, and 51% when β = 0.1. As with the single RC line, it was found that the effect of pre-emphasis pulsing increases as β decreases. Fig. 17 shows T_{opt} and t_{delay_min} as a function of α for (a) $C_c/C_g = 0.25$, (b) $C_c/C_g = 1$, and (c) $C_c/C_g = 4$ on the three general RC lines. The vertical axis is normalized by t_{delay_min} with α = 1 in the case of a step pulse. The errors are within 6.7% in Fig. 17(a), 2.1% in Fig. 17(b), and 2.8% in Fig. 17(c), respectively, when α ≥ 1.1. When the case of α = 1.6 is compared, the delay time is reduced by 72% when $C_c/C_g = 0.25$, by 69% when $C_c/C_g = 1$, and 71% when $C_c/C_g = 4$. It is noted that the effect of pre-emphasis pulsing did not change much when the ratio of C_c to C_g changed.

3.3 Impact of Random Variation on Delay Time

Process variations include line-to-line variation and random within-delay-line variation. In this sub-section, the impact of random variation is examined. Figure 18 shows the ef-

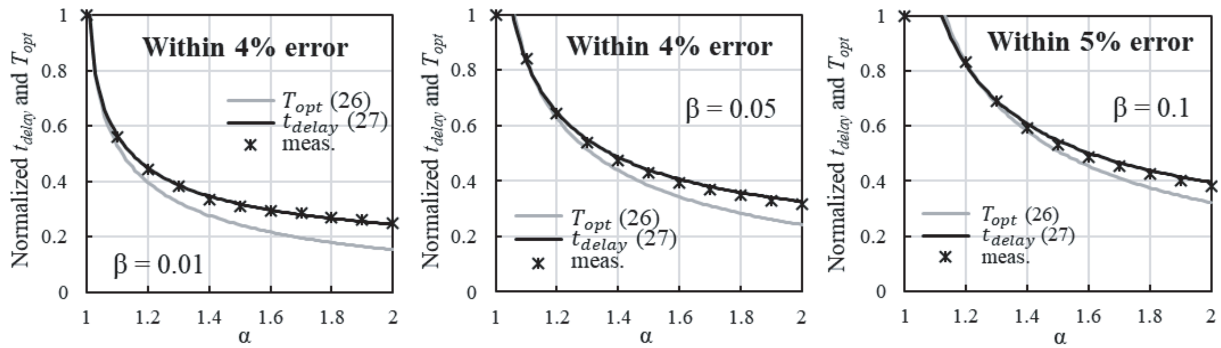

(a): β = 0.01 (b): β = 0.05 (c): β = 0.1

Fig. 16 Verification of t_{delay} in capacitive coupling RC lines.

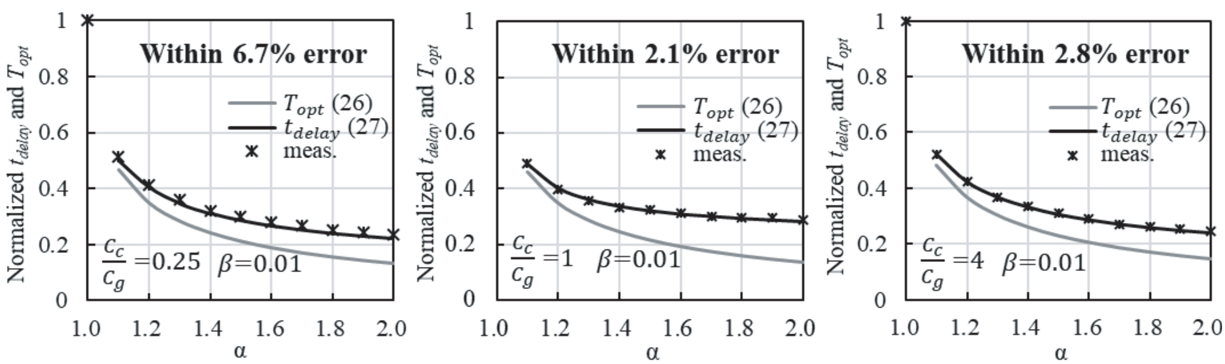

(a): $C_c/C_g = 0.25$ (b): $C_c/C_g = 1$ (c): $C_c/C_g = 4$

Fig. 17 Verification of t_{delay} in the general three RC lines.

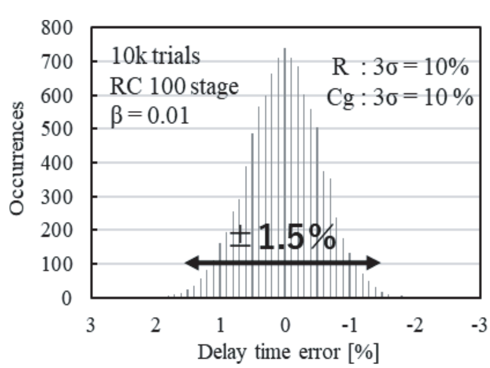

Fig. 18 Effect of the variation for each element on the delay time.

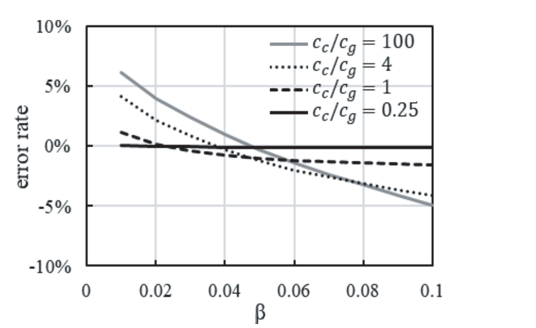

Fig. 19 Comparison of error in delay time between three-line and five-line models.

fect of the variation on the delay time of each element in a 100-stage single RC line using Monte Carlo simulation. The input is a step pulse. The process variation is assumed to be 3σ = 10% for both R and C_g using a normal distribution. With 10k runs, the error range was within ±1.5%. As a result, the influence of the variation in the delay line is small enough to design the optimum pulse.

3.4 Validity of Three-Lines Equivalent Circuit

There are many lines adjacent each other in the memory and the display. In this paper, we ignored the effect of more lines and used a three lines equivalent circuit. This section examines the effect of adjacent lines. Figure 19 shows comparison of delay times by SPICE when step waveforms are input to the three-line and five-line models. The vertical axis is the error of the delay time of three-lines with five-lines. Comparisons of C_c/C_g = 100, 4, 1 and 0.25 were performed. Even in the extreme case of C_c/C_g = 100, the error rate is within 6.2% for the range of 0.01 ≤ β ≤ 0.1. When C_c/C_g = 1, the error rate is within 1.5% for the range of 0.01 ≤ β ≤ 0.1. Because $C_c/C_g \le 1$ nominally, it is validated that the three-line model is sufficient to discuss delay time.

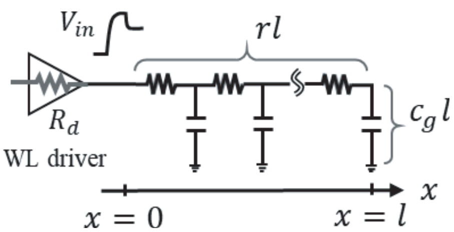

Fig. 20 Equivalent circuit with driver resistance.

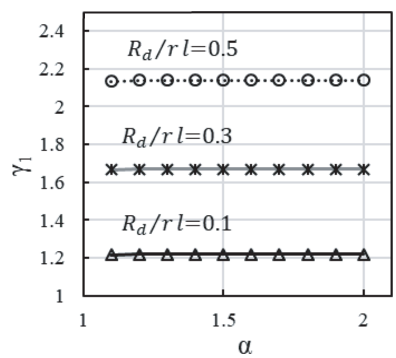

Fig. 21 Optimal γ_1 for each α.

3.5 Design with Driver Resistance

The output resistance of the pre-emphasis driver can be designed to be sufficiently smaller than rl. In a NAND, the WL is selected by a decoding transistor. The on-resistance R_d may not be sufficiently smaller than the WL resistance because the size of the decoding transistor is limited according to the WL pitch. Therefore, in this section, we consider a circuit model that includes a driver resistance as shown in Fig. 20 for a pre-emphasis pulse design. In [15], the optimum value was shown by approximate calculation, but the accuracy was not sufficient. For example, when $R_d/rl = 0.5$, the error exceeded 50%. Therefore, in this section, an empirical formula is presented based on SPICE simulation. Let's assume that (26) and (27) are valid even with the presence of R_d. Fig. 21 shows γ_1 for $\beta = 0.01$. Since γ_1 does not change, even when α changes, it can be confirmed that γ_1 is not a function of α. The horizontal axis of Fig. 21 is changed to R_d/rl for Fig. 22. The plot in Fig. 22 shows the average of the optimum values of γ_1 from $\alpha = 1.1$ to $\alpha = 2.0$ obtained by SPICE simulation. γ_1 varies linearly with respect to R_d/rl. Therefore, γ_1 can be expected to be a linear function on R_d/rl. Considering that $\gamma_1 = 1$ at $R_d/rl = 0$, it can be predicted that $\gamma_1 = \mathrm{a} \times (R_d/rl) + 1$ with a proportional coefficient "a". Using the least squares method within the range of $R_d/rl \leq 0.5$, "a" was determined to be 2.25 as in (28). The value was updated to be more precise from the result in [15] which was 2.

$$\gamma_1 = 2.25\frac{\mathrm{R_d}}{\mathrm{rl}} + 1 \tag{28}$$

Equation (28) is plotted in Fig. 22. As shown, (28) agreed

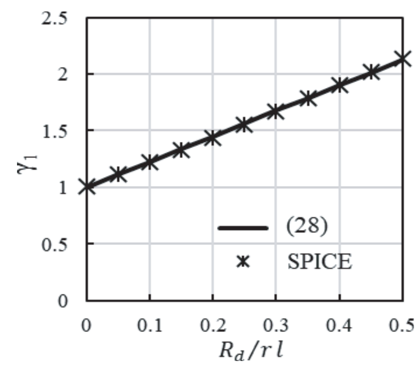

Fig. 22 Optimal γ_1 for each R_d/rl.

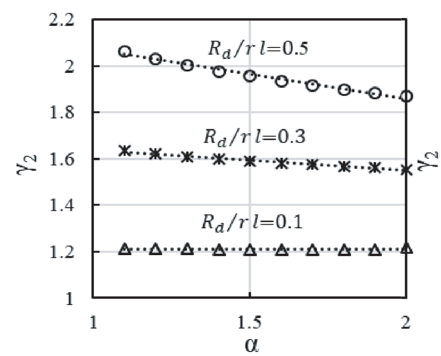

Fig. 23 Optimal γ_2 for each α.

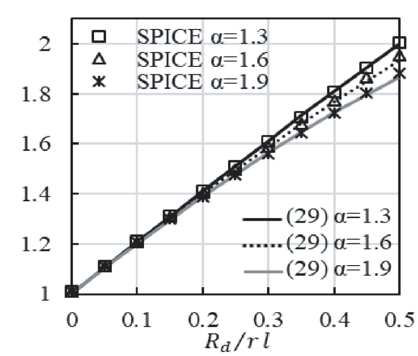

Fig. 24 Optimal γ_2 for each R_d/rl.

with the SPICE simulation within 0.9% error with $\beta = 0.01$, $R_d/rl \leq 0.5$, and $1.1 \leq \alpha \leq 2.0$. Next, an empirical formula for γ_2 is determined. Figure 23 shows the optimum value of γ_2 obtained from the SPICE simulation when α is changed. When α changes, the value of γ_2 changes linearly, indicating a linear function of α. In Fig. 24, the horizontal axis of Fig. 23 is changed to R_d/rl. Since the value of γ_2 changes nonlinearly when R_d/rl changes, it can be seen that it is not a linear function of R_d/rl and the intercept is 1. Based on these results, various approximation functions were tried. One example is (29).

$$\gamma_2 = -0.9\left(\frac{R_d}{rl}\right)^2(\alpha - 1.1) + 2.1\left(\frac{R_d}{rl}\right) + 1 \tag{29}$$

Table 4 Main results of this work.

	1) Single RC line with R_d=0	2) General three RC lines with R_d=0 (β=0.01)	3) Capacitive coupling RC lines with R_d=0	4) Single RC line model with $R_d > 0$
γ_1	1	Table I	1.5	$2.25\frac{R_d}{rl}+1$ (28)
γ_2	1	Table II	1.5	$-0.9\left(\frac{R_d}{rl}\right)^2(\alpha-1.1)+2.1\left(\frac{R_d}{rl}\right)+1$ (29)
τ_4	$4r(c_c+c_g)l^2/\pi^2$			
T_{opt}	$\gamma_1\tau_4\ln\frac{\alpha}{\alpha-1}$ (26)			
t_{delay_min}	$\gamma_2\frac{\tau_4}{9}\ln\left[\frac{4\alpha}{3\pi\beta}\left(\frac{\alpha}{\alpha-1}\right)^8\right]$ (27)			

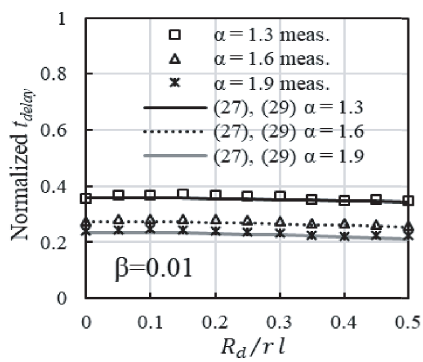

Fig. 25 Verification of t_{delay} when including R_d.

(29) is plotted in Fig. 24. Equation (29) agreed with the SPICE simulation within 1.3% error with β = 0.01, $R_d/rl \le 0.5$, and $1.1 \le \alpha \le 2.0$. Figure 25 shows t_{delay} as a function of R_d/rl for β = 0.01 on a single RC line with driver resistance. The vertical axis is normalized by t_{delay} with α = 1 in case of a step pulse. Equations (28) and (29) are in good agreement with the measurement; they are within 5. 7% error with β = 0.01, $R_d/rl \le 0.5$ and $1.3 \le \alpha \le 1.9$. When the case of α = 1.6 is compared, the delay time is reduced by 72% when R_d/rl = 0.1, and 74% when R_d/rl = 0.5. It is noted that the effect of pre-emphasis pulsing increases slightly as R_d/rl increases. In this study, we made an empirical formula in a wide range of $R_d/rl \le 0.5$ so that it can be used in many practical cases. Note that the coefficients in (28) and (29) are valid within the above errors as far as $1.1 \le \alpha \le 2.0$ and β = 0.01, but the approximation formula must be updated if the range in β is reduced to ≤ 1%.

3.6 Summary

Table 4 summarizes T_{opt} and t_{delay_min} in case of 1) single RC line with $R_d = 0$, 2) general three RC lines with $R_d = 0$, 3) capacitive coupling RC lines with $R_d = 0$, and 4) Single RC line model with $R_d > 0$. 1), 3) and 4) were presented in [15]. 4) was updated in this paper with more precise fitting. 2) is the main contribution of this work, which includes 1) and 3). One can design a pre-emphasis pulse with parameters γ_1 and γ_2 in Tables 1 and 2. Based on Tables 1 and 2, one can use a single line model for Cc/Cg < 0.5 whereas capacitive-coupling model for Cc/Cg > 10. General three-line model must be used for 0.5 < Cc/Cg < 10. Based on Figs. 22 and 24, the impact of Rd on the pre-emphasis pulse width and the resultant delay time must be considered severely when R_d/rl > 5% which provides discrepancy in T_{opt} and t_{delay_min} by 10% or more in comparison with the case that R_d is negligibly small.

4. Conclusion

In this paper, we formulated a pre-emphasis pulsing formula to reduce the delay time of an RC delay line. The formula can be applied to design flat-panel displays and 3D NANDs. The calculation procedure was presented to have the exact solutions of the voltage waveform for a single RC line and three general RC lines. The optimum value that minimizes the delay time was derived by numerical calculation for three general RC lines. An empirical formula was derived based on the simulation results for the optimum value when the driver resistance was not neglected. The results are summarized in Table 4. By using Table 4, the circuit designer can easily estimate the minimum delay condition and delay time at the initial design phase for various RC delay line circuits.

Acknowledgments

The authors would like to thank VDEC, Synopsys, Inc., Cadence Design Systems, Inc., Rohm Corp. and Micron Foundation for their support. The authors appreciate reviewers' valuable feedback to the original manuscript.

References

[1] A. Fiedler R. Mactaggart, J. Welch, and S. Krishnan, "A 1.0625-Gb/s transceiver with 2 oversampling and transmit signal pre-emphasis,"

IEEE International Solids-State Circuits Conference, pp.238–239, Feb. 1997.
[2] J.S. Bang, H.S. Kim, K.S. Yoon, S.H. Lee, S.H. Park, O. Kwon, C. Shin, S. Kim, and G.H. Cho, “A load-aware pre-emphasis column driver with 27% settling-time reduction in ±18% panel-load RC delay variation for 240 Hz UHD flat-panel displays,” IEEE International Solids-State Circuits Conference, Feb. 2016.
[3] W. Jeong, J. Im, D.H. Kim, S.W. Nam, D.K. Shim, M.H. Choi, H.J. Yoon, D.H. Kim, Y.S. Kim, H.W. Park, D.H. Kwak, S.W. Park, S.M. Yoon, W.G. Hahn, J.H. Ryu, S.W. Shim, K.T. Kang, J.D. Ihm, I.M. Kim, D.S. Lee, J.H. Cho, M.S. Kim, J.H. Jang, S.W. Hwang, D.S. Byeon, H.J. Yang, K. Park, K.H. Kyung, and J.H. Choi, “A 128 Gb 3b/cell V-NAND flash memory with 1 Gb/s I/O rate,” IEEE J. Solid-State Circuits, vol.51, no.1, pp.204–212, Jan. 2016.
[4] T. Tanzawa, T. Murakoshi, T. Kamijo, T. Tanaka, J.J. McNeil, and K. Duesman, “Design challenge in 3D NAND technology: A 4.8X area- and 1.3X power-efficient 20 V charge pump using tier capacitors,” IEEE Asian Solid-State Circuits Conference, Nov. 2016.
[5] G.G. Marotta, A. Macerola, A. D’Alessandro, A. Torsi, C. Cerafogli, C. Lattaro, C. Musilli, D. Rivers, E. Sirizotti, F. Paolini, G. Imondi, G. Naso, G. Santin, L. Botticchio, L. De Santis, L. Pilolli, M.L. Gallese, M. Incarnati, M. Tiburzi, P. Conenna, S. Peru, V. Moschiano, W.D. Francesco, M. Goldman, C. Haid, D.D. Cicco, D. Orlandi, F. Rori, M. Rossini, T. Vali, R. Ghodsi, and F. Roohparvar, “A 3 bit/Cell 32 Gb NAND flash memory at 34 nm with 6 MB/s program throughput and with dynamic 2b/cell blocks configuration mode for a program throughput increase up to 13 MB/s,” IEEE International Solids-State Circuits Conference, Feb. 2010.
[6] W.C. Elmore, “The transient response of damped linear networks with particular regard to wideband amplifiers,” J. Appl. Phys., vol.19, no.1, pp.55–63, 1948.
[7] G. Deily, “Closed-form solutions for voltage-step response of open and shorted distributed RC lines,” IEEE Trans. Circuits Syst., vol.22, no.6, pp.534–541, June 1975.
[8] T. Sakurai, “Approximation of wiring delay in MOSFET LSI,” IEEE J. Solid-State Circuits, vol.SC-18, no.4, pp.418–426, Aug. 1983.
[9] T. Sakurai, “Closed-form expressions for interconnection delay, coupling, and crosstalk in VLSI’s,” IEEE Trans. Electron Devices, vol.40, no.1, pp.118–124, Jan. 1993.
[10] H. Kawaguchi and T. Sakurai, “Delay and noise formulas for capacitively coupled distributed RC lines,” Proc. 1998 Asia and South Pacific Design Automation Conference, pp.35–43, 1998,
[11] M. Madec, L. Hebrard, J.-B. Kammerer, M. Madec, L. Hébrard, J.B. Kammerer, A. Bonament, E. Rosati, and C. Lallement, “Multiphysics simulation of biosensors involving 3D biological reaction–diffusion phenomena in a standard circuit EDA environment,” IEEE Trans. Circuits Syst. I, Reg. Papers, vol.66, no.6, pp.2188–2197, June 2019.
[12] R.K.H. Galvao, S. Hadjiloucas, K.H. Kienitz, H.M. Paiva, and R.J.M. Afonso, “Fractional order modeling of large three-dimensional RC networks,” IEEE Trans. Circuits Syst. I, Reg. Papers, vol.60, no.3, pp.624–637, March 2013.
[13] R.K.H. Galvão, S. Hadjiloucas, K.H. Kienitz, et al., “Detecting compositional changes in dielectric materials simulated by three-dimensional RC network models,” IEEE Trans. Dielectr. Electr. Insul., vol.24, no.2, pp.624–37, Nov. 2017.
[14] W. Mitkowski, “Finite-dimensional approximations of distributed RC networks,” Bulletin of the Polish Academy of Sciences Technical Sciences, vol.62, no.2, pp.263–269, Feb. 2014.
[15] K. Matsuyama and T. Tanzawa, “Design of pre-emphasis pulses for large memory arrays with minimal word-line delay time,” IEEE International Symposium on Circuits and Systems (ISCAS), May 2019.
[16] K. Matsuyama and T. Tanzawa, “A pre-emphasis pulse generator insensitive to process variation for driving large memory and panel display arrays with minimal delay time,” IEEE Asia Pacific Conference on Circuits and Systems (APCCAS), pp.45–48, Nov. 2019.

Appendix A: Calculation Procedure for Single RC Line

This section explains the process of deriving (3) (4) from (1) and (2). First, the waveform when $t \le T_{pre}$ is formulated. The Laplace transform of (1) and (2) gives (A1) and (A2), respectively.

$$-\frac{\mathrm{d}E(x,s)}{dx} = rI(x,s) \tag{A$\cdot$1}$$

$$-\frac{dI(x,s)}{dx} = sc_g E(x,s) - c_g e(x,0) \tag{A$\cdot$2}$$

$E(x,s)$ and $I(x,s)$ are Laplace transforms of $e(x,t)$ and $i(x,t)$ with respect to t. Differentiating both sides of (A· 1) and (A· 2) by x, (A· 3) and (A· 4) are obtained.

$$\frac{d^2E(x,s)}{dx^2} = src_g E(x,s) - c_g re(x,0) \tag{A$\cdot$3}$$

$$\frac{d^2I(x,s)}{dx^2} = src_g I(x,s) + c_g\frac{d}{dx}e(x,0) \tag{A$\cdot$4}$$

When the line is fully discharged at time t = 0, $e(x,0) = 0$, so the general solutions of (A· 3) and (A· 4) are

$$E(x,s) = A(s)\mathrm{e}^{-r(s)x} + B(s)e^{r(s)x} \tag{A$\cdot$5}$$

$$I(x,s) = \frac{A(s)e^{-r(s)x} - B(s)e^{r(s)x}}{Z_0(s)} \tag{A$\cdot$6}$$

where $Z_0(s)$ is a characteristic impedance $Z_0(s) = \sqrt{r/sc_g}$, and $r(s) = \sqrt{rc_g s}$. When $\mathrm{t} \le \mathrm{T}_{\mathrm{pre}}$, $E(0,s) = \alpha\mathrm{E}/\mathrm{s}$ and $I(l,s) = 0$. Thus A(s) and B(s) can be solved as

$$A(s) = \frac{\alpha E}{s}\frac{-e^{r(s)l}}{-e^{r(s)l} - e^{-r(s)l}} \tag{A$\cdot$7}$$

$$B(s) = \frac{\alpha E}{s}\frac{-e^{-r(s)l}}{-e^{r(s)l} - e^{-r(s)l}} \tag{A$\cdot$8}$$

Using (A· 7) and (A· 8), (A· 6) becomes (A· 9).

$$E(x,s) = \frac{\alpha E}{s}\frac{\cosh\left[r(s)(l-x)\right]}{\cosh[r(s)l]} \tag{A$\cdot$9}$$

The inverse Laplace transform of (A· 9) is determined to be

$$e(x,t) = \alpha E\left\{1 - \frac{4}{\pi}\sum_{k=0}^{\infty}\frac{1}{2k+1}e^{\frac{-(2k+1)^2\pi^2}{4rc_g l^2}t}sin\frac{(2k+1)\pi}{2l}x\right\}$$

$$\mathrm{t} \le \mathrm{T}_{\mathrm{pre}} \tag{A$\cdot$10}$$

Next, the waveform when $\mathrm{t} > \mathrm{T}_{\mathrm{pre}}$ is formulated. Consider $e'(x,t')$, $i'(x,t')$ such that $t' = t - T_{pre}$. Thus, it can be considered that the pulse goes down from αE to E at $t' = 0$. The same equation as (A· 3) is valid for $E'(x,s)$ and $e'(x,t')$ resulting in (A · 3′).

$$\frac{d^2E'(x,s)}{dx^2} = src_g E'(x,s) - c_g re'(x,0) \tag{A$\cdot$3$'$}$$

Since $e'(x,0) = e\left(x, T_{pre}\right)$, (A· 11) results in (A· 12).

$$\frac{d^2E'(x,s)}{dx^2} - r^2(s)E'(x,s) = -rc_g\alpha E\left\{1 - \frac{4}{\pi}\sum_{k=0}^{\infty}\frac{1}{2k+1}e^{\frac{-(2k+1)^2\pi^2}{4rc_gl^2}T_{pre}}sin\frac{(2k+1)\pi}{2l}x\right\} \tag{A· 11}$$

(A· 11) is further calculated individually using the principle of superposition. (A· 11) can be decomposed into the following three equations.

$$\frac{d^2E'(x,s)}{dx^2} - r^2(s)E'(x,s) = 0 \tag{A· 12}$$

$$\frac{d^2E'(x,s)}{dx^2} - r^2(s)E'(x,s) = -rc_g\alpha E \tag{A· 13}$$

$$\frac{d^2E'(x,s)}{dx^2} - r^2(s)E'(x,s) = \sum_{k=0}^{\infty}Q(k)sinN(k)x \tag{A· 14}$$

where

$$Q(k) = \frac{4rc_g\alpha E}{\pi}\frac{1}{2k+1}e^{\frac{-(2k+1)^2\pi^2}{4rc_gl^2}T_{pre}}$$

$$N(k) = \frac{(2k+1)\pi}{2l}$$

Since (A· 12) is identical to (A· 3), the general solution of (A· 12) is the same as (A· 5). Since (A· 13) has a constant on the right side, its particular solution can be easily obtained as

$$E'(x,s) = \frac{\alpha E}{s} \tag{A· 15}$$

Next, consider (A· 14). The particular solution of (A· 14) can be predicted using C (s) as follows

$$E'(x,s) = \sum_{k=0}^{\infty}C(s)sinN(k)x \tag{A· 16}$$

Substituting (A· 16) into (A· 14) and comparing the coefficients of $sinN(k)x$, $C(s)$ is obtained as

$$C(s) = \frac{Q(k)}{N(k)^2 + r(s)^2} \tag{A· 17}$$

Summing up these equations gives (A· 18)

$$E'(x,s) = A(s)e^{-r(s)x} + B(s)e^{r(s)x} + \frac{\alpha E}{s} - \sum_{k=0}^{\infty}\frac{Q(k)}{N(k)^2 + r(s)^2}sinN(k)x \tag{A· 18}$$

The same equation as (A· 1) is valid for $E'(x,s)$ and $I'(x,s)$ resulting in (A · 1′).

$$-\frac{\mathrm{d}E'(x,s)}{dx} = rI'(x,s) \tag{A · 1′}$$

Deriving $I'(x,s)$ using (A · 1′) and (A· 19),

$$I'(x,s) = \frac{A(s)e^{-r(s)x} - B(s)e^{r(s)x}}{Z_0(s)} + \frac{1}{r}\sum_{k=0}^{\infty}\frac{Q(k)N(k)}{N(k)^2 + r(s)^2}cosN(k)x \tag{A· 19}$$

When $t > T_{pre}$, $E'(0,s) = E/s$ and $I'(l,s) = 0$, so $A(s)$ and B(s) can be solved as

$$\mathrm{A}(s) = \frac{(1-\alpha)E}{s}\frac{-e^{r(s)l}}{-e^{r(s)l} - e^{-r(s)l}} \tag{A· 20}$$

$$\mathrm{B}(s) = \frac{(1-\alpha)E}{s}\frac{-e^{-r(s)l}}{-e^{r(s)l} - e^{-r(s)l}} \tag{A· 21}$$

(A· 18) becomes (A· 22) with (A· 20) and (A· 21).

$$E'(x,s) = \frac{(1-\alpha)E}{s}\frac{\cosh[r(s)(l-x)]}{\cosh[r(s)l]} + \frac{\alpha E}{s} - \sum_{k=0}^{\infty}\frac{Q(k)}{N(k)^2 + r(s)^2}sinN(k)x \tag{A· 22}$$

When the inverse Laplace transforms and converts (A· 22) to a function of t using $t' = t - T_{pre}$, one can obtain (A· 23)

$$e(x,t) = E + \frac{4E}{\pi}\sum_{k=0}^{\infty}\left\{(\alpha-1)e^{\frac{(2k+1)^2\pi^2}{4rc_gl^2}T_{pre}}\alpha\right\} \cdot\frac{1}{2k+1}e^{\frac{-(2k+1)^2\pi^2}{4rc_gl^2}t}sin\frac{(2k+1)\pi x}{2l} \quad \mathrm{t} > T_{pre} \tag{A· 23}$$

When one sets $\tau_1 = 4rc_gl^2/\pi^2$, (3) and (4) are obtained from (A· 10) and (A· 23), respectively.

Appendix B: Calculation Procedure for General RC Lines

This section explains the process of deriving (24) and (25) from (20), (21), (22) and (23). First, the waveform when $\mathrm{t} \le \mathrm{T_{pre}}$ is formulated. Laplace transform of (20), (21), (22) and (23) give (A· 24), (A· 25), (A· 26) and (A· 27), respectively.

$$-\frac{dE_1(x,s)}{dx} = rI_1(x,s) \tag{A· 24}$$

$$-\frac{dE_2(x,s)}{dx} = \frac{1}{2}rI_2(x,s) \tag{A· 25}$$

$$-\frac{dI_1(x,s)}{dx} = s\left(c_c + c_g\right)E_1(x,s) - sc_cE_2(x,s) - \left(c_c + c_g\right)e_1(x,0) + c_ce_2(x,0) \tag{A· 26}$$

$$-\frac{dI_2(x,s)}{dx} = -sc_cE_1(x,s) + s\left(c_c + 2c_g\right)E_2(x,s) + c_ce_1(x,0) - \left(c_c + 2c_g\right)e_2(x,0) \tag{A· 27}$$

$E_1(x,s)$, $E_2(x,s)$, $I_1(x,s)$ and $I_2(x,s)$ are Laplace transforms of $e_1(x,t)$, $e_2(x,t)$, $i_1(x,t)$ and $i_2(x,t)$ with respect to t. Differentiating both sides of (A· 24) and (A· 25) by x, (A· 28) is obtained.

$$\ddot{\vec{\boldsymbol{E}}} = sr\boldsymbol{D}\vec{\boldsymbol{E}} - r\boldsymbol{D}\vec{\boldsymbol{e}}(x,0) \tag{A· 28}$$

$$\boldsymbol{D} = \begin{pmatrix} c_c + c_g & -c_c \\ -\frac{c_c}{2} & \frac{c_c + 2c_g}{2} \end{pmatrix}$$

$$\vec{\boldsymbol{E}} = \begin{pmatrix} E_1(x,s) \\ E_2(x,s) \end{pmatrix}, \quad \vec{\boldsymbol{e}}(x,0) = \begin{pmatrix} e_1(x,0) \\ e_2(x,0) \end{pmatrix}$$

$\boldsymbol{D}$ can be diagonalized using $\boldsymbol{R} = \begin{pmatrix} 2 & 1 \\ -1 & 1 \end{pmatrix}$ and $\boldsymbol{R}^{-1} = \frac{1}{3}\begin{pmatrix} 1 & -1 \\ 1 & 2 \end{pmatrix}$ as follows

$$\boldsymbol{R}^{-1}\boldsymbol{D}\boldsymbol{R} = \begin{pmatrix} 1.5c_1 + c_2 & 0 \\ 0 & c_2 \end{pmatrix} \tag{A·29}$$

Using $A_1(s)$, $A_2(s)$, $B_1(s)$, $B_2(s)$ and initial condition $e_1(x,0) = e_2(x,0) = 0$, the general solution of (A·28) is

$$\begin{aligned} \vec{\boldsymbol{E}}(x,s) &= \boldsymbol{R}\begin{pmatrix} A_1(s)e^{r_1(s)x} & 0 \\ 0 & A_2(s)e^{r_2(s)x} \end{pmatrix}\boldsymbol{R}^{-1}\vec{\boldsymbol{E}}(0,s) \\ &+\boldsymbol{R}\begin{pmatrix} B_1(s)e^{-r_1(s)x} & 0 \\ 0 & B_2(s)e^{-r_2(s)x} \end{pmatrix}\boldsymbol{R}^{-1}\vec{\boldsymbol{E}}(0,s) \end{aligned} \tag{A·30}$$

where $r_1(s) = \sqrt{sr(1.5c_c + c_g)}$ and $r_2(s) = \sqrt{src_g}$. Substituting the conditions of $E_1(0,s) = \alpha E/s$ and $E_2(0,s) = 0$,

$$\begin{aligned} E_1(x,s) &= \frac{2}{3}\frac{\alpha E}{s}\left(A_1(s)e^{r_1(s)x} + B_1(s)e^{-r_1(s)x}\right) \\ &+ \frac{1}{3}\frac{\alpha E}{s}\left(A_2(s)e^{r_2(s)x} + B_2(s)e^{-r_2(s)x}\right) \end{aligned} \tag{A·31}$$

$$\begin{aligned} E_2(x,s) &= -\frac{1}{3}\frac{\alpha E}{s}\left(A_1(s)e^{r_1(s)x} + B_1(s)e^{-r_1(s)x}\right) \\ &+ \frac{1}{3}\frac{\alpha E}{s}\left(A_2(s)e^{r_2(s)x} + B_2(s)e^{-r_2(s)x}\right) \end{aligned} \tag{A·32}$$

$I_1(x,s)$ and $I_2(x,s)$ are obtained from (A·24), (A·25), (A·31) and (A·32).

$$\begin{aligned} I_1(x,s) &= \frac{2}{3}\frac{\alpha E}{s}\left(A_1(s)e^{r_1(s)x} - B_1(s)e^{-r_1(s)x}\right)\frac{r_1(s)}{r} \\ &+ \frac{1}{3}\frac{\alpha E}{s}\left(A_2(s)e^{r_2(s)x} - B_2(s)e^{-r_2(s)x}\right)\frac{r_2(s)}{r} \end{aligned} \tag{A·33}$$

$$\begin{aligned} I_2(x,s) &= -\frac{2}{3}\frac{\alpha E}{s}\left(A_1(s)e^{r_1(s)x} - B_1(s)e^{-r_1(s)x}\right)\frac{r_1(s)}{r} \\ &+ \frac{2}{3}\frac{\alpha E}{s}\left(A_2(s)e^{r_2(s)x} - B_2(s)e^{-r_2(s)x}\right)\frac{r_2(s)}{r} \end{aligned} \tag{A·34}$$

When $t \leq T_{pre}$, $E_1(0,s) = \alpha E/\mathrm{s}$, $E_2(0,s) = 0$, $I_1(l,s) = 0$, and $I_2(l,s) = 0$. Thus, $A_1(s)$, $A_2(s)$, $B_1(s)$ and $B_2(s)$ can be solved as

$$A_1(s) = \frac{e^{-r_1(s)l}}{e^{r_1(s)l} + e^{-r_1(s)l}} \tag{A·35}$$

$$B_1(s) = \frac{e^{r_1(s)l}}{e^{r_1(s)l} + e^{-r_1(s)l}} \tag{A·36}$$

$$A_2(s) = \frac{e^{-r_2(s)l}}{e^{r_2(s)l} + e^{-r_2(s)l}} \tag{A·37}$$

$$B_2(s) = \frac{e^{r_2(s)l}}{e^{r_2(s)l} + e^{-r_2(s)l}} \tag{A·38}$$

From these equations, (A·31) and (A·32) result in

$$E_1(x,s) = \frac{2}{3}\frac{\alpha E}{s}\frac{\cosh\left[r_1(s)(l-x)\right]}{\cosh\left[r_1(s)l\right]} + \frac{1}{3}\frac{\alpha E}{s}\frac{\cosh\left[r_2(s)(l-x)\right]}{\cosh\left[r_2(s)l\right]} \tag{A·39}$$

$$E_2(x,s) = -\frac{1}{3}\frac{\alpha E}{s}\frac{\cosh\left[r_1(s)(l-x)\right]}{\cosh\left[r_1(s)l\right]} + \frac{1}{3}\frac{\alpha E}{s}\frac{\cosh\left[r_2(s)(l-x)\right]}{\cosh\left[r_2(s)l\right]} \tag{A·40}$$

The inverse Laplace transform of (A·39) and (A·40) are obtained as

$$\begin{aligned} e_1(x,t) &= \alpha E - \frac{8\alpha E}{3\pi}\sum_{k=0}^{\infty}\frac{1}{2k+1}e^{\frac{-(2k+1)^2\pi^2}{4r(1.5c_c+c_g)l^2}t}\, sin\frac{(2k+1)\pi}{2l}x \\ &- \frac{4\alpha E}{3\pi}\sum_{k=0}^{\infty}\frac{1}{2k+1}e^{\frac{-(2k+1)^2\pi^2}{4rc_gl^2}t}\, sin\frac{(2k+1)\pi}{2l}x \end{aligned} \tag{A·41}$$

$$\begin{aligned} e_2(x,t) &= \frac{4\alpha E}{3\pi}\sum_{k=0}^{\infty}\frac{1}{2k+1}e^{\frac{-(2k+1)^2\pi^2}{4r(1.5c_c+c_g)l^2}t}\, sin\frac{(2k+1)\pi}{2l}x \\ &- \frac{4\alpha E}{3\pi}\sum_{k=0}^{\infty}\frac{1}{2k+1}e^{\frac{-(2k+1)^2\pi^2}{4rc_gl^2}t}\, sin\frac{(2k+1)\pi}{2l}x \end{aligned} \tag{A·42}$$

Next, the waveform when $t > T_{pre}$ is formulated. Consider $e_1'(x,t')$, $e_2'(x,t')$, $i_1'(x,t')$ and $i_2'(x,t')$ such that $t' = t - T_{pre}$. Thus, it can be considered that the pulse goes down from αE to E at $t' = 0$. When $\begin{pmatrix} e_1'(x,0) \\ e_2'(x,0) \end{pmatrix} = \vec{e'}(x,0)$ is used, (A·28) becomes

$$\ddot{\vec{\mathbf{E}'}} = sr\boldsymbol{D}\vec{\mathbf{E}'} - r\boldsymbol{D}\vec{\mathbf{e}'}(x,0) \tag{A·43}$$

Substituting $\vec{e'}(x,0) = \begin{pmatrix} e_1\left(x, T_{pre}\right) \\ e_2\left(x, T_{pre}\right) \end{pmatrix}$, (A·43) becomes

$$\begin{aligned} &\ddot{\vec{\mathbf{E}'}} - sr\boldsymbol{D}\vec{\mathbf{E}'} = \\ &-r\boldsymbol{D}\left\{\begin{pmatrix} \alpha E \\ 0 \end{pmatrix} + \begin{pmatrix} -2\sum_{k=0}^{\infty}Q_1(k)sinN(k)x - \sum_{k=0}^{\infty}Q_2(k)sinN(k)x \\ \sum_{k=0}^{\infty}Q_1(k)sinN(k)x - \sum_{k=0}^{\infty}Q_2(k)sinN(k)x \end{pmatrix}\right\} \end{aligned} \tag{A·44}$$

$$Q_1(k) = \frac{4\alpha E}{3\pi}\frac{1}{2k+1}e^{\frac{-(2k+1)^2\pi^2}{4r(1.5c_c+c_g)l^2}T_{pre}}$$

$$Q_2(k) = \frac{4\alpha E}{3\pi}\frac{1}{2k+1}e^{\frac{-(2k+1)^2\pi^2}{4rc_gl^2}T_{pre}}$$

$$N(k) = \frac{(2k+1)\pi}{2l}$$

(A·44) can be solved individually using the principle of superposition. (A·44) can be decomposed into the following three equations.

$$\ddot{\vec{\mathbf{E}}} - sr\boldsymbol{D}\vec{\mathbf{E}} = 0 \tag{A·45}$$

$$\ddot{\vec{\mathbf{E}}} - sr\boldsymbol{D}\vec{\mathbf{E}} = -r\boldsymbol{D}\begin{pmatrix} \alpha E \\ 0 \end{pmatrix} \tag{A·46}$$

$$\begin{aligned} &\ddot{\vec{\mathbf{E}}} - sr\boldsymbol{D}\vec{\mathbf{E}} = \\ &-r\boldsymbol{D}\begin{pmatrix} -2\sum_{k=0}^{\infty}Q_1(k)sinN(k)x - \sum_{k=0}^{\infty}Q_2(k)sinN(k)x \\ \sum_{k=0}^{\infty}Q_1(k)sinN(k)x - \sum_{k=0}^{\infty}Q_2(k)sinN(k)x \end{pmatrix} \end{aligned} \tag{A·47}$$

Since (A· 45) is identical to (A· 28), the solution of (A· 45) is the same as (A· 31). Since (A· 46) has a constant on the right side, its particular solution can be easily obtained as

$$\vec{\mathrm{E}} = \begin{pmatrix} \frac{\alpha E}{s} \\ 0 \end{pmatrix} \tag{A· 48}$$

The particular solution of (A· 47) can be predicted using $A_3(s)$ and $B_3(s)$ as follows

$$\vec{\mathrm{E}'} = \begin{pmatrix} \sum_{k=0}^{\infty} A_3(s) sin N(k) x \\ \sum_{k=0}^{\infty} B_3(s) sin N(k) x \end{pmatrix} \tag{A· 49}$$

Substituting (A· 49) into (A· 47) and comparing the coefficients of $sinN(k)x$, $A_3(s)$ is obtained as

$$A_3(s) = \frac{-2r\left(1.5c_c + c_g\right)Q_1}{N^2 + sr\left(1.5c_c + c_g\right)} + \frac{-rc_g Q_2}{\left(N^2 + src_g\right)} \tag{A· 50}$$

$B_3(s)$ is not necessary for deriving $e_1(x,t)$. Summing up these equations gives (A· 51) and (A· 52).

$$\begin{aligned} E_1'(x,s) = &\frac{2}{3}\frac{E}{s}\left(A_1'(s)e^{r_1(s)x} + B_1'(s)e^{-r_1(s)x}\right) \\ &+ \frac{1}{3}\frac{E}{s}\left(A_2'(s)e^{r_2(s)x} + B_2'(s)e^{-r_2(s)x}\right) + \frac{\alpha E}{s} \\ &+ \sum_{k=0}^{\infty} A_3(s) sin \frac{(2k+1)\pi}{2l}x \end{aligned} \tag{A· 51}$$

$$\begin{aligned} E_2'(x,s) = &-\frac{1}{3}\frac{E}{s}\left(A_1'(s)e^{r_1(s)x} + B_1'(s)e^{-r_1(s)x}\right) \\ &+ \frac{1}{3}\frac{E}{s}\left(A_2'(s)e^{r_2(s)x} + B_2'(s)e^{-r_2(s)x}\right) \\ &+ \sum_{k=0}^{\infty} B_3(s) sin \frac{(2k+1)\pi}{2l}x \end{aligned} \tag{A· 52}$$

Deriving $I_1'(x,s)$ and $I_2'(x,s)$ using similar equations to (A· 24) and (A· 25) yields.

$$\begin{aligned} I_1'(x,s) = &\frac{2}{3}\frac{\alpha E}{s}\left(A_1'(s)e^{\mathrm{r}_1(s)x} - B_1'(s)e^{-\mathrm{r}_1(s)x}\right)\frac{r_1(s)}{r} \\ &+ \frac{1}{3}\frac{\alpha E}{s}\left(A_2'(s)e^{\mathrm{r}_2(s)x} - B_2'(s)e^{-\mathrm{r}_2(s)x}\right)\frac{r_2(s)}{r} \\ &+ \frac{1}{r}\sum_{k=0}^{\infty}\frac{d}{dx}A_3(s) sin \frac{(2k+1)\pi}{2l}x \end{aligned} \tag{A· 53}$$

$$\begin{aligned} I_2'(x,s) = &-\frac{1}{3}\frac{\alpha E}{s}\left(A_1'(s)e^{\mathrm{r}_1(s)x} - B_1'(s)e^{-\mathrm{r}_1(s)x}\right)\frac{2r_1(s)}{r} \\ &+ \frac{1}{3}\frac{\alpha E}{s}\left(A_2'(s)e^{\mathrm{r}_2(s)x} - B_2'(s)e^{-\mathrm{r}_2(s)x}\right)\frac{2r_2(s)}{r} \\ &+ \frac{2}{r}\sum_{k=0}^{\infty}\frac{d}{dx}B_3(s) sin \frac{(2k+1)\pi}{2l}x \end{aligned} \tag{A· 54}$$

When $t > T_{pre}$, $E_1'(0,s) = E/s$, $E_2'(0,s) = 0$, $I_1'(l,s) = 0$ and $I_2'(l,s) = 0$ hold. Thus, $A_1'(s)$, $A_2'(s)$, $B_1'(s)$ and $B_2'(s)$ can be solved as

$$A_1'(s) = (1-\alpha)\frac{e^{-r_1(s)l}}{e^{r_1(s)l} + e^{-r_1(s)l}} \tag{A· 55}$$

$$B_1'(s) = (1-\alpha)\frac{e^{r_1(s)l}}{e^{r_1(s)l} + e^{-r_1(s)l}} \tag{A· 56}$$

$$A_2'(s) = (1-\alpha)\frac{e^{-r_2(s)l}}{e^{r_2(s)l} + e^{-r_2(s)l}} \tag{A· 57}$$

$$B_2'(s) = (1-\alpha)\frac{e^{r_2(s)l}}{e^{r_2(s)l} + e^{-r_2(s)l}} \tag{A· 58}$$

Summarizing the previous formulas, (A· 51) becomes (A· 59).

$$\begin{aligned} E_1'(x,s) \; = \; &\frac{2}{3}\frac{(1-\alpha)E}{s}\frac{\cosh\left[r_1(s)(l-x)\right]}{\cosh\left[r_1(s)l\right]} \\ &+\frac{1}{3}\frac{(1-\alpha)E}{s}\frac{cosh\left[r_2(s)(l-x)\right]}{cosh\left[r_2(s)l\right]} + \frac{\alpha E}{s} \\ &- \sum_{k=0}^{\infty}\frac{Q_1(k)}{\frac{(2k+1)^2\pi^2}{4r\left(1.5c_c+c_g\right)l^2} + s} sin \frac{(2k+1)\pi}{2l}x \\ &- \sum_{k=0}^{\infty}\frac{Q_2(k)}{\frac{(2k+1)^2\pi^2}{4rc_g l^2} + s} sin \frac{(2k+1)\pi}{2l}x \end{aligned} \tag{A· 59}$$

When (A· 59) is transformed and converted by the inverse Laplace transformed and converted to a function of t using $t' = t - T_{pre}$, one can obtain (A· 60).

$$\begin{aligned} e_1(x,t) \; = \; &E - \frac{2}{3}\frac{4E}{\pi}\sum_{k=0}^{\infty}\left\{\alpha - (\alpha - 1)e^{\frac{(2k+1)^2\pi^2}{4r(1.5c_c+c_g)l^2}T_{pre}}\right\} \\ &\cdot\frac{1}{2k+1}e^{\frac{-(2k+1)^2\pi^2}{4r(1.5c_c+c_g)l^2}t} sin \frac{(2k+1)\pi}{2l}x \\ &-\frac{1}{3}\frac{4E}{\pi}\sum_{k=0}^{\infty}\left\{\alpha - (\alpha-1)e^{\frac{(2k+1)^2\pi^2}{4rc_g l^2}T_{pre}}\right\} \\ &\cdot\frac{1}{2k+1}e^{\frac{-(2k+1)^2\pi^2}{4rc_g l^2}t} sin \frac{(2k+1)\pi}{2l}x \end{aligned} \tag{A· 60}$$

When one sets $\tau_3 = 4r\left(1.5c_c + c_g\right)l^2/\pi^2$ and $\tau_1 = 4rc_g l^2/\pi^2$, (24) and (25) are obtained from (A· 41) and (A· 60), respectively.

Kazuki Matsuyama received the B.E. and M.E. degrees in Electrical Engineering from Shizuoka University in 2018 and 2020, respectively. He is now with FUJI Corp.

Toru Tanzawa received the B.S. degree in physics from Saitama University, Saitama, Japan, in 1990, the M.S. degree in physics from Tohoku University, Sendai, Japan, in 1992, and the Ph.D. degree in electrical engineering from The University of Tokyo, Tokyo, Japan, in 2002. In 1992, he joined the Toshiba Research and Development Center, Japan. He had worked on the circuit design of high-density NAND Flash memories and high-speed low-voltage NOR Flash memories for ten years and on the circuit design of RF-CMOS wireless LSIs for Bluetooth for the following three years. From 2004 to 2017, he was with Micron Japan, Ltd., Tokyo, where he has worked on MLC NAND Flash design at the Japan Flash Design Center. He is a professor with Faculty of Engineering, Shizuoka University Dr. Tanzawa holds 260 U.S. patents and has published 48 papers in IEEE conferences and journals. Toru Tanzawa is a Fellow of IEEE.